

Authigenic mineral phases as a driver of the upper-ocean iron cycle

<https://doi.org/10.1038/s41586-023-06210-5>

Received: 18 November 2022

Accepted: 12 May 2023

Published online: 2 August 2023

 Check for updates

Alessandro Tagliabue^{1✉}, Kristen N. Buck^{2,3}, Laura E. Sofen⁴, Benjamin S. Twining⁴, Olivier Aumont⁵, Philip W. Boyd⁶, Salvatore Caprara², William B. Homoky⁷, Rod Johnson⁸, Daniela König^{1,†}, Daniel C. Ohnemus⁹, Bettina Sohst¹⁰ & Peter Sedwick¹⁰

Iron is important in regulating the ocean carbon cycle¹. Although several dissolved and particulate species participate in oceanic iron cycling, current understanding emphasizes the importance of complexation by organic ligands in stabilizing oceanic dissolved iron concentrations^{2–6}. However, it is difficult to reconcile this view of ligands as a primary control on dissolved iron cycling with the observed size partitioning of dissolved iron species, inefficient dissolved iron regeneration at depth or the potential importance of authigenic iron phases in particulate iron observational datasets^{7–12}. Here we present a new dissolved iron, ligand and particulate iron seasonal dataset from the Bermuda Atlantic Time-series Study (BATS) region. We find that upper-ocean dissolved iron dynamics were decoupled from those of ligands, which necessitates a process by which dissolved iron escapes ligand stabilization to generate a reservoir of authigenic iron particles that settle to depth. When this ‘colloidal shunt’ mechanism was implemented in a global-scale biogeochemical model, it reproduced both seasonal iron-cycle dynamics observations and independent global datasets when previous models failed^{13–15}. Overall, we argue that the turnover of authigenic particulate iron phases must be considered alongside biological activity and ligands in controlling ocean-dissolved iron distributions and the coupling between dissolved and particulate iron pools.

Iron (Fe) is an essential element that governs microbial activity over much of the ocean and, by means of its influence on the biological carbon pump, modulates the carbon cycle¹. For instance, past changes in Fe supply to the ocean during glacial periods are invoked as a driver of fluctuations in atmospheric carbon dioxide levels¹⁶. On the early Earth, low oxygen levels meant that Fe was abundant and thus used as a catalyst for several cellular processes in marine phytoplankton, including photosynthesis and respiration^{17,18}. As the ocean became oxygenated, ferrous Fe (Fe²⁺) was oxidized to form ferric (Fe³⁺) (oxyhydr)oxides, which would have precipitated or adsorbed to particles and thus become lost from the dissolved Fe (DFe) phase (<0.2 μm) that is most bioavailable to marine phytoplankton¹. Complexation of ferric Fe by organic molecules, known as ligands, has been thought to stabilize DFe by preventing loss through oxidative precipitation, thereby regulating ocean DFe concentrations². This relatively simple hypothesis has been invoked to explain observations of Fe in the ocean interior^{3,5,6}, the ocean carbon cycle¹⁹ and the balance between ocean Fe and nitrogen limitation⁴. Syntheses of available ligand and DFe data have shown that ligand concentrations are usually well in excess of DFe (refs. 20–22), implying that the complexation capacity of Fe-binding ligands is often undersaturated. However, this finding is at odds with

estimates of substantial DFe removal rates along water mass transport pathways and limited net solubilization of DFe from remineralization of sinking particulate Fe (PFe)^{7,8,10,23–25}. Global ocean Fe models, parameterized to represent ligand control of DFe, also tend to perform poorly against large-scale ocean DFe datasets^{13,14}, indicating that our current understanding cannot accurately constrain the ocean Fe cycle. This knowledge gap undermines confidence in projections of the impacts of environmental change in Fe-limited ocean regions²⁶.

Authigenic mineral phases are known to play an important role in the cycling of Fe in the Earth system, but have—so far—been largely ignored as a driver of the contemporary ocean Fe cycle¹. Oxidation of Fe(II) to Fe(III) in natural waters precipitates colloidal-sized (approximately 0.02–0.2 μm) Fe (CFe) (oxyhydr)oxides, such as nano-ferrihydrate, nano-goethite and nano-haematite, which may also sorb organic carbon functional groups²⁷ and undergo further aggregation to form sinking authigenic PFe (>0.2 μm). Authigenic Fe phases are commonly invoked as substantial components of external iron inputs from rivers, sediments, icebergs and hydrothermal vents (for example, refs. 28–30) and CFe may comprise 50% or more of the ocean DFe pool, depending on the environmental setting^{31,32}. Yet, despite their ubiquity, how aggregation of colloidal iron oxides to form sinking authigenic PFe and regulate Fe

¹School of Environmental Sciences, University of Liverpool, Liverpool, UK. ²College of Marine Science, University of South Florida, St. Petersburg, FL, USA. ³College of Earth, Ocean, and Atmospheric Sciences, Oregon State University, Corvallis, OR, USA. ⁴Bigelow Laboratory for Ocean Sciences, East Boothbay, ME, USA. ⁵LOCEAN, IRD-CNRS-Sorbonne Université-MNHN, IPSL, Paris, France. ⁶Institute for Marine and Antarctic Studies, University of Tasmania, Hobart, Tasmania, Australia. ⁷School of Earth and Environment, University of Leeds, Leeds, UK. ⁸Bermuda Institute of Ocean Sciences, St. George's, Bermuda. ⁹Skidaway Institute of Oceanography, University of Georgia, Department of Marine Sciences, Savannah, GA, USA. ¹⁰Department of Ocean and Earth Sciences, Old Dominion University, Norfolk, VA, USA. [†]Present address: Department of Oceanography, School of Ocean and Earth Science and Technology, University of Hawai'i at Mānoa, Honolulu, HI, USA. ✉e-mail: a.tagliabue@liverpool.ac.uk

cycling alongside ligand stabilization is unknown, especially as Fe is not equally exchanged between the colloidal and ligand-bound dissolved pools^{11,12}. In the particulate phase, authigenic Fe phases can be important⁹ and have been estimated to account for as much as 40% of total PFe in the South Pacific¹⁰ and Ross Sea³³. Care is needed when deriving large-scale corrections for lithogenic PFe, but an examination of chemically labile PFe observations from the recent GEOTRACES Intermediate Data Product 2021 (IDP2021) suggests that between half and three-quarters of samples have PFe that cannot be accounted for as biogenic PFe (typically assumed to be the main labile pool; see Methods). Taken together, these observations imply that we may be neglecting a crucial component in our understanding of the ocean Fe cycle.

A critical challenge in Earth science is to quantify the response of ocean systems to environmental change. This is particularly acute for Fe, which has a short residence time and is thus responsive to rapid alterations to ocean physics and atmospheric inputs (for example, from anthropogenic activity³⁴ and wildfires³⁵). Although the database of oceanic DFe observations has grown markedly during the multidecadal GEOTRACES global survey, we lack insight into concurrent temporal variations in DFe, ligand-bound Fe and PFe (Supplementary Table 1), which constitute a robust test for hypotheses about the mechanisms driving the Fe cycle (for example, refs. 7,36). The degree to which DFe inventories are controlled by ligands and/or authigenic phases is not testable with currently available data. Addressing this issue is important because it hampers our understanding of the mechanisms that drive oceanic Fe distributions and therefore the ocean carbon cycle and marine ecosystems. Here we report a new seasonal-scale Fe observational dataset (the Bermuda Atlantic Iron Time-series, BAIT) comprising the parallel seasonal evolution of DFe, ligands and PFe phases in the BATS region of the Sargasso Sea, designed to explore these drivers in an integrated fashion for the first time. Together, these data yield a new conceptual and numerical model of the ocean Fe cycle that uniquely reconciles the roles of biological activity, ligands and authigenic phases, with important implications for the global ocean Fe and carbon cycles.

Seasonal dissolved iron and ligand variations

We conducted fieldwork in March, May, August and November 2019, sampling the BATS site and two adjacent spatial stations to approximately 1,800 m depth each time and observed a pronounced seasonal cycle in the upper-ocean DFe inventory, consistent with previous observations¹⁵. Aeolian deposition drove an increase in surface DFe concentrations from low levels (about 0.08–0.22 nM) in late winter (March) to values over 1.5 nM in late summer (August), decreasing to around 0.5 nM by autumn (November; Fig. 1). Notably, despite the subtropical location of the BATS region, these low winter DFe concentrations are more typical of the strongly Fe-limited Southern Ocean³⁷. In contrast to the upper ocean, there was little seasonal change below depths of about 1,000 m, at which DFe concentrations remained around 0.75–1 nM (Fig. 1), similar to other regional datasets^{15,38,39}. Integrated over the upper 200 m that encompasses the seasonal thermocline, DFe inventories increase almost threefold, from 30 $\mu\text{mol m}^{-2}$ in March to 70 $\mu\text{mol m}^{-2}$ in August, before decreasing to just below 50 $\mu\text{mol m}^{-2}$ in November (Fig. 2a). Horizontal changes during this study, driven by the regional eddy field¹⁵, were small relative to the seasonal dynamics (as seen by the strong similarity and low standard error across the three profiles per voyage). Consistent with its location in the North Atlantic subtropical gyre, net biological removal of Fe at the BATS site is low⁴⁰.

Notably, high turnover in the DFe inventories took place against the backdrop of a strong excess Fe complexation capacity in both total and stronger Fe-binding ligands. In the upper 200 m, we provide the first evidence that concentrations of total and strong Fe-binding ligands (L_T and L_S , respectively; see Methods) consistently exceeded DFe concentrations by about 3 nM and about 1 nM, respectively, throughout the year (Extended Data Figs. 1 and 2). Below 1,000 m, the excesses in stronger

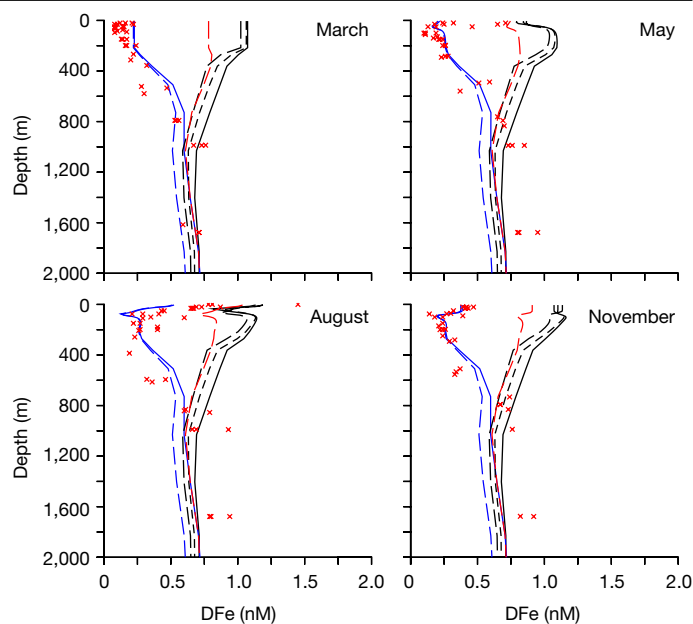


Fig. 1 | Seasonal evolution of DFe. DFe data and model solutions at the BATS site for March, May, August and November. Red crosses are DFe data for each voyage for three stations in the BATS region. Solid and dashed black lines are model solutions at the BATS site from the standard PISCES-Quota model, with varying total ligands derived from DOC (using 0.09, 0.08 and 0.07 nM L_T ($\mu\text{M DOC}^{-1}$) or, shown by dashed red lines, with prognostic stronger ligands (see Methods). Blue lines represent model solutions from the new PISCES-Quota-Fe model accounting for iron oxides and authigenic phases, with either prognostic stronger ligands (solid blue lines; see Methods) or DOC-derived total ligands (dashed blue lines, using 0.09 nM L_T ($\mu\text{M DOC}^{-1}$)).

ligands dropped below 0.5 nM, whereas those of the weaker total ligands remained more than 1 nM above DFe concentrations. Integrated over the upper 200 m, inventories of total and stronger ligands showed much smaller seasonal changes and remained twofold to fivefold in excess of DFe year round (integrated inventories always exceeded 450 or 200 $\mu\text{mol m}^{-2}$ for total and stronger ligands, respectively; Fig. 2a).

This seasonal evolution of DFe and ligands, documented here for the first time, cannot be reproduced by a global ocean model that assumes equilibrium between DFe and ligands. The PISCES-Quota global model accounts for a complex representation of the ocean Fe cycle, including lithogenic particles and ligand stabilization of DFe. Total weaker ligand concentrations were derived from dissolved organic carbon (DOC) or modelled as stronger ligands and matched observations well (Extended Data Fig. 1 and Methods). Thus, the PISCES-Quota model serves as a direct test of whether the seasonal observations of DFe could be reproduced with accurate representation of ligands. Across a range of total ligand-to-DOC ratios or with stronger ligands, PISCES-Quota performed well in reproducing observed DFe concentrations below 1,000 m but systematically overestimated upper-ocean DFe concentrations (black lines in Fig. 1).

All PISCES-Quota model experiments failed to generate sufficient excesses in total or stronger ligands, relative to observations (Extended Data Fig. 2), because greater concentrations of ligands in the model lead to excessive DFe. Comparing the modelled seasonal variations in the inventories of DFe and ligands side by side, we find that a strong link emerges (Fig. 2c), as expected from the posited conceptual coupling of DFe and ligands⁴. However, the observed contemporaneous evolution of the DFe and ligand inventories do not conform to this expectation (for either stronger or total weaker ligands; Fig. 2c). This indicates that an assumed equilibrium between ligands and DFe is not compatible with our observations in the upper water column. This poor skill

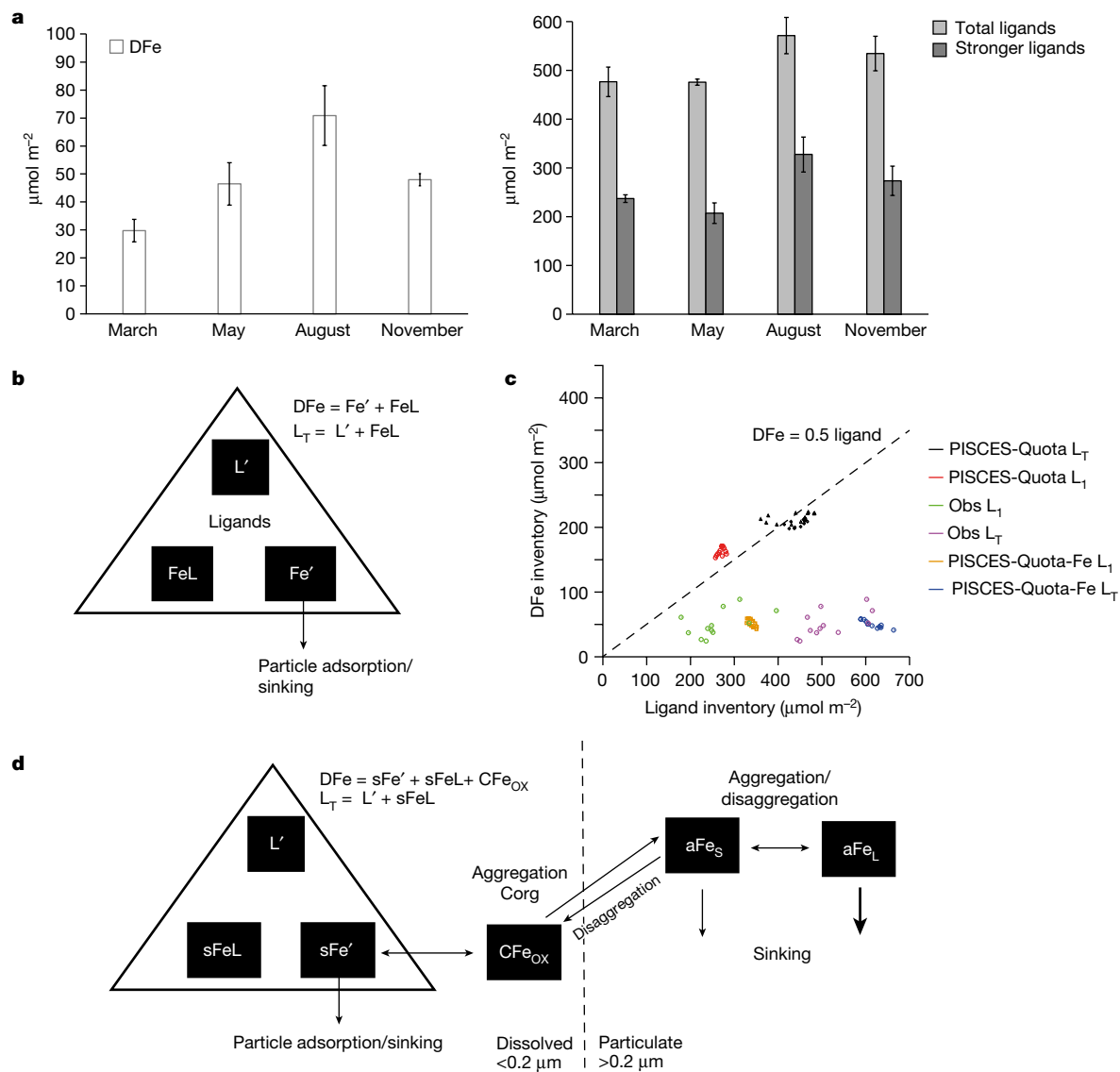


Fig. 2 | Observations and modelling of DFe and ligand dynamics. **a**, Seasonal evolution of DFe and L_T or L_1 in the upper 200 m from observations ($\mu\text{mol m}^{-2}$; error bars represent standard errors across the three stations). **b**, Schematic of the PISCES-Quota model, with all of the DFe pool in equilibrium with ligands (as FeL). **c**, The cross plot of the seasonal evolution of weaker total ligands (L_T , purple) or stronger ligands (L_1 , green) and DFe in the upper 200 m. Black symbols represent the solution of the PISCES-Quota model with varying total ligands derived from DOC (using 0.09, 0.08 and 0.07 $\text{nM } L_T$ ($\mu\text{M DOC}^{-1}$) or prognostic stronger ligands (red), whereas orange symbols represent the solution of the PISCES-Quota-Fe model with prognostic stronger ligands

and blue symbols represent the solution of the PISCES-Quota-Fe model with DOC-derived total ligands (using 0.09 $\text{nM } L_T$ ($\mu\text{M DOC}^{-1}$)). The dashed line represents the 0.5:1 DFe:ligand line. **d**, Schematic of the new PISCES-Quota-Fe model, in which only soluble Fe (sFe) is in equilibrium with ligands (as sFeL) and Fe (oxyhydr)oxides (CFe_{ox}) aggregate with organic carbon (Corg) to form small and large authigenic Fe particles (aFe_S and aFe_L , respectively). The triangles in panels **b** and **d** represent the portion of the DFe pool in equilibrium with ligands. The vertical dashed line in panel **d** represents the boundary between DFe ($<0.2 \mu\text{m}$) and PFe ($>0.2 \mu\text{m}$).

for DFe is not unusual for global ocean Fe models⁸, but its persistence here implies that it does not arise from errors in the representation of Fe-binding ligands. Moreover, alternative approaches, such as applying greater scavenging rate on DFe by lithogenic particles suggested previously⁴¹, does not improve the model–observation fit either (Extended Data Fig. 3) and biological removal of iron is low (see below). This suggests that the prevailing Fe–ligand stabilization theory is insufficient to explain our new observations.

Reconciling observations and models

To reconcile our observations, we advance a new conceptual model that decouples the cycling of Fe through CFe (oxyhydr)oxides from dissolved

organic ligands, building on ideas developed for thorium⁴². However, instead of assuming that metals adsorb onto colloidal organic matter, we focus here on the aggregation of CFe (oxyhydr)oxides: CFe is observed to be a notable component of DFe, often making up more than 50% in our samples and accumulated seasonally in the upper 200 m (similar to other work in this region^{31,32,43}). Unlike the few previous models that include CFe (ref. 44) or explore dissolved-particulate partitioning⁴⁵, and in agreement with estimates from thermodynamic partitioning work^{11,12} and porewater modelling²⁹, we assume that CFe (part of the $<0.2 \mu\text{m}$ DFe pool) is not chemically complexed by ligands. Instead, CFe is considered to comprise Fe oxyhydroxide minerals that aggregate with bulk labile DOC to produce small authigenic particles that aggregate into larger authigenic particles (both within the $>0.2 \mu\text{m}$ PFe pool),

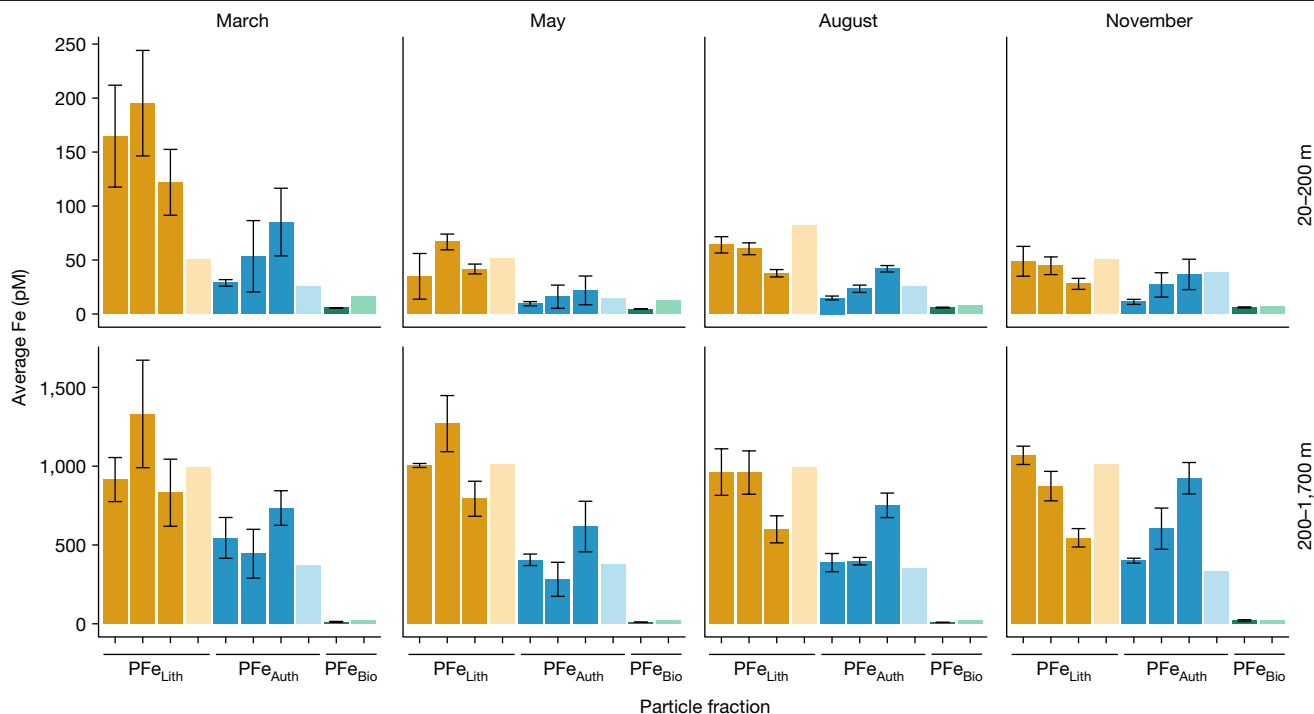


Fig. 3 | Seasonal evolution of PFe phases. Lithogenic, authigenic and biogenic PFe phases (PFe_{Lith} , PFe_{Auth} and PFe_{Bio} , respectively). Lithogenic PFe (in orange) is estimated by means of three approaches (from left bar to right bar: refractory PFe, using particulate Al and a local Fe:Al ratio and using particulate Al and a standard upper continental crust Fe:Al ratio; see Methods). Biogenic PFe (in green) is estimated using observed Fe cell quotas by means of particulate phosphorus. Authigenic PFe (in blue) is calculated as the residual

from $PFe - PFe_{Lith} - PFe_{Bio}$, with the three estimates spanning the three different PFe_{Lith} estimates. Darker coloured bars are observations and corresponding lighter coloured bars are the solution of the PISCES-Quota-Fe model with prognostic stronger ligands at the BATS site for each of the months concerned. The error bars on the observations represent the standard error across the three stations sampled during each cruise.

which then sink and cycle independently of ligand-bound DFe (see Methods; Fig. 2d). As previously, ligand dynamics in this new model assume either prescribed weaker total ligands or prognostically simulated stronger ligands driven by specific source–sink dynamics (either approach fits observations well; Extended Data Fig. 1; see Methods). Our new PISCES-Quota-Fe model shows a markedly improved ability to reproduce our seasonal observations of DFe (Fig. 1), excess ligands (Extended Data Fig. 2) and the evolution of upper 200 m DFe and ligand inventories (Fig. 2c). These improvements are noteworthy considering the dynamics of the seasonal cycle at the BATS site, particularly the excellent fit by season and depth, compared with previous efforts^{13–15}. Overall, PISCES-Quota-Fe results were insensitive to whether we chose to model total weaker or stronger ligands. This indicates that, although ligands are critical to stabilize the soluble ($<0.02 \mu\text{m}$) portions of the DFe pool, further mechanisms are required to explain the fate of CFe. Greater emphasis on the cycling of CFe (oxyhydr)oxides and authigenic Fe minerals (as part of the PFe pool) as first-order drivers of the upper-ocean DFe cycle is required.

Observed and modelled authigenic PFe concentrations provide further support for the importance of CFe cycling. An important corollary of our new conceptual viewpoint is that, if CFe (oxyhydr)oxides are not in equilibrium with organic Fe-binding ligands, then authigenic PFe should accumulate alongside the more commonly considered lithogenic and biogenic PFe pools. We measured total PFe in samples from each BAIT voyage and derived the authigenic contribution by subtracting the lithogenic and biogenic components of PFe, using a variety of approaches (see Methods)¹⁰. Overall, between 15–56% and 20–62% of the total PFe was authigenic (that is, not accounted for by biogenic or lithogenic pools) in the upper 200 m and the 200–2,000 m depth strata, respectively (Fig. 3), consistent with limited previous indications¹⁰. Notably, estimates of lithogenic, biogenic and authigenic PFe from

our new PISCES-Quota-Fe global model closely match observations, in terms of overall magnitude, seasonal changes and the increase in authigenic PFe with depth (Fig. 3). This further model–data convergence bolsters our hypothesis about the importance of Fe cycling through a ‘colloidal shunt’ of CFe (oxyhydr)oxides that are not in equilibrium with DFe-binding organic ligands. The small magnitude of the biogenic PFe pool also emphasizes the key role for non-biogenic processes in regulating the upper-ocean Fe inventory.

Globally, PISCES-Quota-Fe shows improved skill for both DFe and PFe observations. Across $>10,000$ and $>1,500$ observations for DFe and PFe, respectively, PISCES-Quota shows a reduced bias and a better correlation and slope, both throughout the water column and in the upper 200 m (Extended Data Table 1 and Extended Data Fig. 4). PISCES-Quota-Fe is also able to retain the existing skill of the PISCES-Quota model in reproducing the distributions of a broad suite of biogeochemical tracers, including nutrients, oxygen, chlorophyll and particulate organic carbon (POC) export (Extended Data Fig. 5), similar to other Earth system models⁴⁶.

A new view of global ocean Fe cycling

The upper-ocean Fe cycle modulates biological activity and the biological carbon pump. Our results reveal a delicate balance between ligand stabilization, biological cycling by the ‘ferrous wheel’ and abiotic cycling through authigenic phases by means of the newly emphasized ‘colloidal shunt’ in regulating upper-ocean Fe cycling (Fig. 4a). Their relative role can be quantified using our new PISCES-Quota-Fe model (Fig. 4, using discrete inventories). Where biological activity is high (for example, parts of the Southern Ocean or eastern boundary upwelling systems), the biological ferrous wheel dominates (about 23% of the ocean surface area), as in previous studies⁷. Where total

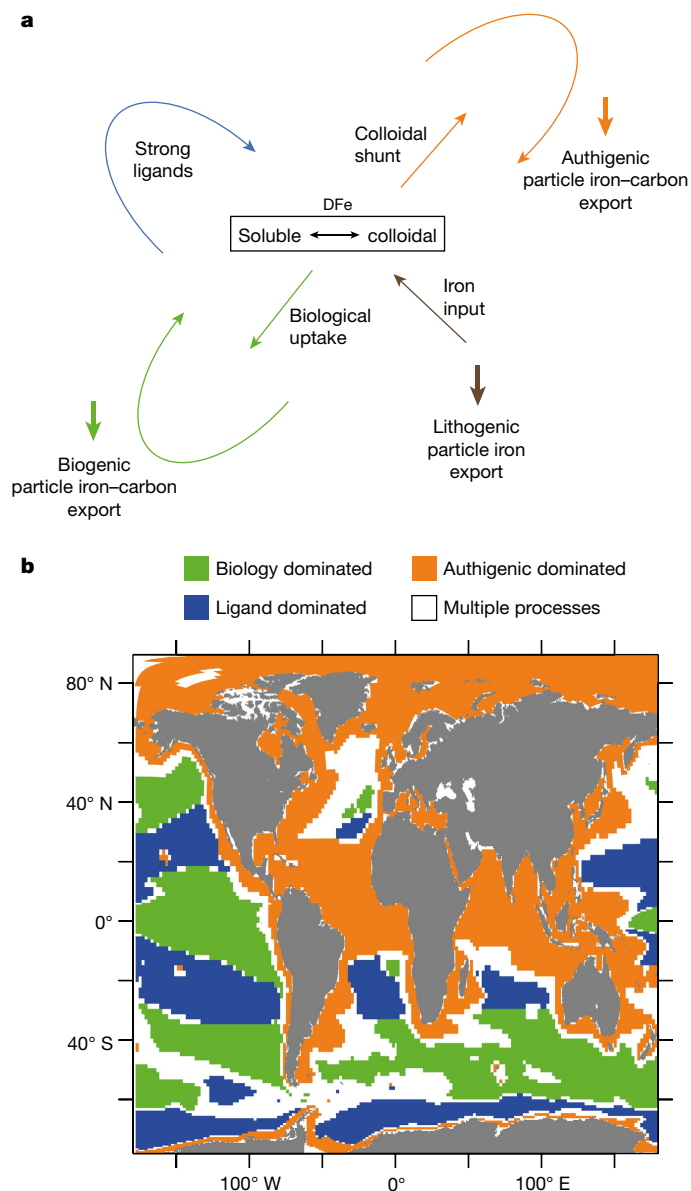


Fig. 4 | An integrated view of the ocean iron cycle. a, A schematic illustrating how the biological uptake (green: sum of diatom, picophytoplankton, nanophytoplankton, microzooplankton, mesozooplankton and organic PFe), ligand stabilization (blue: sum of organically complexed and free DFe) and the colloidal shunt (orange: sum of colloidal iron (oxyhydr)oxides and small and large authigenic particle Fe) maintain surface ocean Fe levels. **b,** Model quantifications of the dominant term at each location in the upper 100 m using the new PISCES-Quota-Fe model in the same colours, with white areas denoting regions in which more than one process dominates.

Fe concentrations and biological activity are lower (for example, the remote oligotrophic gyres of the Pacific Ocean), ligand stabilization of Fe dominates (about 18% of the ocean surface area). Wherever Fe inputs are increased (for example, below the Saharan dust plume or along the Antarctic coastline), Fe is predominantly cycled through the colloidal shunt (about 40% of the ocean surface area). In around one-fifth of the surface ocean (white areas), multiple processes are important. Overall, a mosaic of factors compete for available Fe in the surface ocean. In the ocean interior, scavenging and regeneration are usually considered as the dominant drivers^{10,23,38}. However, our results introduce Fe (oxyhydr)oxide aggregation and authigenic PFe disaggregation as further key sinks and sources of DFe, respectively,

especially in the interior of the Atlantic and Southern oceans, in which they reach or exceed 50% of the total Fe source or sink fluxes (Extended Data Fig. 6). The balance between authigenic PFe production and dissolution will dictate how much of the authigenic particle export, initiated by the colloidal shunt, replenishes deep-ocean DFe levels or is removed to the sediments. Further constraints on the underlying processes will improve our understanding of their relative magnitudes and sensitivity to change.

Authigenic Fe phases in the open ocean are probably dominated by mixed Fe (oxyhydr)oxides, including ferrihydrite, goethite and magnetite^{28,47,48}. Understanding how these, and potentially other mineral phases, may contribute to differences in the reactivity, solubility and affinity for organic carbon will illuminate their contribution to ocean Fe and carbon cycling. This will be especially true if the findings from marine sediments and porewaters that organic carbon stabilizes Fe (oxyhydr)oxide colloids²⁹ and that Fe minerals enhance preservation of organic carbon (ref. 49) also apply in the water column. Resolving these questions requires further experimental and process study efforts, integrated with ocean modelling, to deliver the missing mechanistic understanding. Although Fe (oxyhydr)oxides form readily in today's oxic ocean, it is possible that, during past or future periods of lower ocean oxygen, the formation of Fe (oxyhydr)oxides would be diminished and the importance of the colloidal shunt may be lessened, with a stronger role for ligands and biological cycling. This new view of the ocean Fe cycle has numerous, far-reaching implications for DFe removal pathways, surface ocean Fe limitation and sediment–ocean coupling and presents new linkages between the Fe and carbon cycles.

Online content

Any methods, additional references, Nature Portfolio reporting summaries, source data, extended data, supplementary information, acknowledgements, peer review information; details of author contributions and competing interests; and statements of data and code availability are available at <https://doi.org/10.1038/s41586-023-06210-5>.

1. Tagliabue, A. et al. The integral role of iron in ocean biogeochemistry. *Nature* **543**, 51–59 (2017).
2. Gledhill, M. & Buck, K. N. The organic complexation of iron in the marine environment: a review. *Front. Microbiol.* **3**, 69 (2012).
3. Johnson, K. S., Gordon, R. M. & Coale, K. H. What controls dissolved iron concentrations in the world ocean? *Mar. Chem.* **57**, 137–161 (1997).
4. Lauderdale, J. M., Braakman, R., Forget, G., Dutkiewicz, S. & Follows, M. J. Microbial feedbacks optimize ocean iron availability. *Proc. Natl Acad. Sci.* **117**, 4842–4849 (2020).
5. Parekh, P., Follows, M. J. & Boyle, E. A. Decoupling of iron and phosphate in the global ocean. *Glob. Biogeochem. Cycles* **19**, GB2020 (2005).
6. Whitby, H. et al. A call for refining the role of humic-like substances in the oceanic iron cycle. *Sci. Rep.* **10**, 6144 (2020).
7. Boyd, P. W., Ellwood, M. J., Tagliabue, A. & Twining, B. S. Biotic and abiotic retention, recycling and remineralization of metals in the ocean. *Nat. Geosci.* **10**, 167–173 (2017).
8. Frew, R. D. et al. Particulate iron dynamics during FeCycle in subantarctic waters southeast of New Zealand. *Glob. Biogeochem. Cycles* **20**, GB1S93 (2006).
9. Ohnemus, D. C., Torrie, R. & Twining, B. S. Exposing the distributions and elemental associations of scavenged particulate phases in the ocean using basin-scale multi-element data sets. *Glob. Biogeochem. Cycles* **33**, 725–748 (2019).
10. Tagliabue, A. et al. The interplay between regeneration and scavenging fluxes drives ocean iron cycling. *Nat. Commun.* **10**, 4960 (2019).
11. Cullen, J. T., Bergquist, B. A. & Moffett, J. W. Thermodynamic characterization of the partitioning of iron between soluble and colloidal species in the Atlantic Ocean. *Mar. Chem.* **98**, 295–303 (2006).
12. Fitzsimmons, J. N., Bundy, R. M., Al-Subiai, S. N., Barbeau, K. A. & Boyle, E. A. The composition of dissolved iron in the dusty surface ocean: an exploration using size-fractionated iron-binding ligands. *Mar. Chem.* **173**, 125–135 (2015).
13. Tagliabue, A. et al. How well do global ocean biogeochemistry models simulate dissolved iron distributions? *Glob. Biogeochem. Cycles* **30**, 149–174 (2016).
14. Somes, C. J. et al. Constraining global marine iron sources and ligand-mediated scavenging fluxes with GEOTRACES dissolved iron measurements in an ocean biogeochemical model. *Glob. Biogeochem. Cycles* **35**, e2021GB006948 (2021).
15. Sedwick, P. N. et al. Dissolved iron in the Bermuda region of the subtropical North Atlantic Ocean: seasonal dynamics, mesoscale variability, and physicochemical speciation. *Mar. Chem.* **219**, 103748 (2020).
16. Martínez-García, A. et al. Iron fertilization of the Subantarctic Ocean during the last ice age. *Science* **343**, 1347–1350 (2014).

17. Raven, J. A., Evans, M. C. W. & Korb, R. E. The role of trace metals in photosynthetic electron transport in O₂-evolving organisms. *Photosynth. Res.* **60**, 111–150 (1999).
18. Wade, J., Byrne, D. J., Ballentine, C. J. & Drakesmith, H. Temporal variation of planetary iron as a driver of evolution. *Proc. Natl Acad. Sci.* **118**, e2109865118 (2021).
19. Tagliabue, A., Aumont, O. & Bopp, L. The impact of different external sources of iron on the global carbon cycle. *Geophys. Res. Lett.* **41**, 920–926 (2014).
20. Buck, K. N., Sedwick, P. N., Sohst, B. & Carlson, C. A. Organic complexation of iron in the eastern tropical South Pacific: results from US GEOTRACES Eastern Pacific Zonal Transect (GEOTRACES cruise GP16). *Mar. Chem.* **201**, 229–241 (2018).
21. Buck, K. N., Sohst, B. & Sedwick, P. N. The organic complexation of dissolved iron along the U.S. GEOTRACES (GA03) North Atlantic Section. *Deep Sea Res. II Top. Stud. Oceanogr.* **116**, 152–165 (2015).
22. Gerringa, L. J. A., Rijkenberg, M. J. A., Schoemann, V., Laan, P. & de Baar, H. J. W. Organic complexation of iron in the West Atlantic Ocean. *Mar. Chem.* **177**, 434–446 (2015).
23. Bressac, M. et al. Resupply of mesopelagic dissolved iron controlled by particulate iron composition. *Nat. Geosci.* **12**, 995–1000 (2019).
24. Lamborg, C. H. et al. The flux of bio- and lithogenic material associated with sinking particles in the mesopelagic “twilight zone” of the northwest and North Central Pacific Ocean. *Deep Sea Res. II Top. Stud. Oceanogr.* **55**, 1540–1563 (2008).
25. Twining, B. S. et al. Differential remineralization of major and trace elements in sinking diatoms. *Limnol. Oceanogr.* **59**, 689–704 (2014).
26. Tagliabue, A. et al. Persistent uncertainties in ocean net primary production climate change projections at regional scales raise challenges for assessing impacts on ecosystem services. *Front. Clim.* **3**, 738224 (2021).
27. Gunnars, A., Blomqvist, S., Johansson, P. & Andersson, C. Formation of Fe(III) oxyhydroxide colloids in freshwater and brackish seawater, with incorporation of phosphate and calcium. *Geochim. Cosmochim. Acta* **66**, 745–758 (2002).
28. Feely, R. A., Trefry, J. H., Massoth, G. J. & Metz, S. A comparison of the scavenging of phosphorus and arsenic from seawater by hydrothermal iron oxyhydroxides in the Atlantic and Pacific Oceans. *Deep Sea Res. A Oceanogr. Res. Pap.* **38**, 617–623 (1991).
29. Homoky, W. B. et al. Iron colloids dominate sedimentary supply to the ocean interior. *Proc. Natl Acad. Sci.* **118**, e2016078118 (2021).
30. Homoky, W. B. et al. Iron and manganese diagenesis in deep sea volcanogenic sediments and the origins of pore water colloids. *Geochim. Cosmochim. Acta* **75**, 5032–5048 (2011).
31. Fitzsimmons, J. N. & Boyle, E. A. Both soluble and colloidal iron phases control dissolved iron variability in the tropical North Atlantic Ocean. *Geochim. Cosmochim. Acta* **125**, 539–550 (2014).
32. Kunde, K. et al. Iron distribution in the subtropical North Atlantic: the pivotal role of colloidal iron. *Glob. Biogeochem. Cycles* **33**, 1532–1547 (2019).
33. Marsay, C. M., Barrett, P. M., McGillicuddy, D. J. & Sedwick, P. N. Distributions, sources, and transformations of dissolved and particulate iron on the Ross Sea continental shelf during summer. *J. Geophys. Res. Oceans* **122**, 6371–6393 (2017).
34. Conway, T. M. et al. Tracing and constraining anthropogenic aerosol iron fluxes to the North Atlantic Ocean using iron isotopes. *Nat. Commun.* **10**, 2628 (2019).
35. Tang, W. et al. Widespread phytoplankton blooms triggered by 2019–2020 Australian wildfires. *Nature* **597**, 370–375 (2021).
36. Boyd, P. W., Mackie, D. S. & Hunter, K. A. Aerosol iron deposition to the surface ocean – modes of iron supply and biological responses. *Mar. Chem.* **120**, 128–143 (2010).
37. Bowie, A. R. et al. Biogeochemical iron budgets of the Southern Ocean south of Australia: decoupling of iron and nutrient cycles in the subantarctic zone by the summertime supply. *Glob. Biogeochem. Cycles* **23**, GB4034 (2009).
38. Wu, J. & Boyle, E. Iron in the Sargasso Sea: implications for the processes controlling dissolved Fe distribution in the ocean. *Glob. Biogeochem. Cycles* **16**, 33-1–33-8 (2002).
39. Rijkenberg, M. J. et al. The distribution of dissolved iron in the West Atlantic Ocean. *PLoS One* **9**, e101323 (2014).
40. Black, E. E. et al. Ironing out Fe residence time in the dynamic upper ocean. *Glob. Biogeochem. Cycles* **34**, e2020GB006592 (2020).
41. Wagener, T., Gieue, C. & Leblond, N. Effects of dust deposition on iron cycle in the surface Mediterranean Sea: results from a mesocosm seeding experiment. *Biogeosciences* **7**, 3769–3781 (2010).
42. Honeyman, B. D. & Santschi, P. H. A Brownian-pumping model for oceanic trace metal scavenging: evidence from Th isotopes. *J. Mar. Res.* **47**, 951–992 (1989).
43. Wu, J., Boyle, E., Sunda, W. & Wen, L. S. Soluble and colloidal iron in the oligotrophic North Atlantic and North Pacific. *Science* **293**, 847–849 (2001).
44. Völker, C. & Tagliabue, A. Modeling organic iron-binding ligands in a three-dimensional biogeochemical ocean model. *Mar. Chem.* **173**, 67–77 (2015).
45. Misumi, K. et al. Slowly sinking particles underlie dissolved iron transport across the Pacific Ocean. *Glob. Biogeochem. Cycles* **35**, e2020GB006823 (2021).
46. Seferian, R. et al. Tracking improvement in simulated marine biogeochemistry between CMIP5 and CMIP6. *Curr. Clim. Change Rep.* **6**, 95–119 (2020).
47. Raiswell, R., Benning, L. G., Tranter, M. & Tulaczyk, S. Bioavailable iron in the Southern Ocean: the significance of the iceberg conveyor belt. *Geochem. Trans.* **9**, 7 (2008).
48. von der Heyden, B. P., Roychoudhury, A. N., Mtshali, T. N., Tylliszczak, T. & Myneni, S. C. Chemically and geographically distinct solid-phase iron pools in the Southern Ocean. *Science* **338**, 1199–1201 (2012).
49. Curti, L. et al. Carboxyl-richness controls organic carbon preservation during coprecipitation with iron (oxyhydr)oxides in the natural environment. *Commun. Earth Environ.* **2**, 229 (2021).

Publisher's note Springer Nature remains neutral with regard to jurisdictional claims in published maps and institutional affiliations.

Springer Nature or its licensor (e.g. a society or other partner) holds exclusive rights to this article under a publishing agreement with the author(s) or other rightsholder(s); author self-archiving of the accepted manuscript version of this article is solely governed by the terms of such publishing agreement and applicable law.

© The Author(s), under exclusive licence to Springer Nature Limited 2023

Methods

The BAIT programme (GEOTRACES Process Study GApr13) conducted fieldwork as part of the BATS efforts during 2019. Water-column samples for analysis of iron and other trace metals were collected from the BATS site (31° 40' N, 64° 10' W) and adjacent BATS spatial stations during cruises in March (BAIT-I, spring), May (BAIT-II, early summer), August (BAIT-III, late summer) and November (BAIT-IV, autumn) 2019 aboard RV Atlantic Explorer and RV Endeavor. Seawater samples and associated hydrographic data were collected using a trace-metal-clean conductivity–temperature–depth sensor (SBE 19plus, Sea-Bird Electronics) mounted on a custom-built trace-metal-clean carousel (Sea-Bird Electronics) fitted with custom-modified 5-liter Teflon-lined external-closure Niskin-X samplers (General Oceanics) and deployed on an Amsteel non-metallic line. Also, during the August cruise, near-surface samples (roughly 1 m depth) were collected in a Niskin-X sampler that was hand-deployed from an inflatable dinghy about 500 m upwind of the research vessel, to avoid contamination from the ship. On recovery, Niskin-X samplers were transferred into a shipboard Class-100 clean-air laboratory, in which seawater samples were filtered through pre-cleaned 0.2- μm -pore AcroPak Supor filter capsules (Pall) using filtered nitrogen gas⁹.

For DFe analysis, filtrate was collected in acid-cleaned 125-ml low-density polyethylene bottles (Nalgene). For analysis of Fe-binding ligands, filtrate was collected in acid-cleaned and Milli-Q-conditioned fluorinated polyethylene bottles and frozen at 20 °C until analysed at the University of South Florida by competitive ligand exchange–adsorptive cathodic stripping voltammetry²⁰. For soluble Fe (sFe) measurements, the 0.2- μm filtrate was then filtered through dilute-acid-cleaned, sample-rinsed 0.02- μm Anotop syringe filters using a peristaltic pump; the resulting filtrate was stored in acid-cleaned 60-ml low-density polyethylene bottles and acidified to pH 1.7 post-cruise as for DFe samples. For analysis of PFe and other trace metals, 2.35–4.05 liters of seawater were filtered through 25-mm-diameter 0.45- μm polyethersulfone Supor membranes. The filters were cut in half for parallel analysis of labile and total particulate concentrations following the digestion methods of ref. 50, and digested samples were analysed by high-resolution inductively coupled plasma mass spectrometry following published protocols. Cellular iron contents of autotrophic flagellates from 20 m and the deep chlorophyll maximum were analysed following published methods⁵¹ at the Advanced Photon Source, Argonne National Laboratory microprobe beamline 2-ID-E. Our observations of ligands are consistent with previous measurements^{21,22}.

DFe and sFe were determined in the water-column samples using high-resolution inductively coupled plasma mass spectrometry (Thermo Fisher Scientific Element XR) with in-line separation/preconcentration (Elemental Scientific seaFAST-SP3). Calibration standards were prepared in low-iron seawater, for which initial DFe and sFe concentrations were determined using the method of standard additions, with yttrium used as an internal standard. Analytical blank concentrations were assessed by applying the in-line separation/preconcentration procedure including all reagents and loading air in place of the seawater sample ('air blank'), yielding a mean blank concentration that was not statistically different from zero (-0.006 ± 0.0178 nM, $n = 62$); the limit of detection, defined as the concentration equivalent to three times the standard deviation on the mean blank, was 0.054 nM Fe. The mean DFe concentration for ten separate determinations of the GEOTRACES GSP seawater consensus material was 0.177 ± 0.030 nM, which is within analytical uncertainty (1σ) of the current consensus value 0.155 ± 0.045 nM DFe. Estimated analytical precision for DFe at the GSP concentration level is $\pm 17\%$ ($\pm 1\sigma$, $n = 10$) and generally better than $\pm 10\%$ based on repeat determinations for samples with DFe concentrations greater than 0.2 nM. CFe was calculated as the difference between DFe and sFe.

The PFe pool was partitioned into lithogenic, authigenic and biogenic phases using direct measurements of the biogenic fraction, Al tracer

to estimate the lithogenic fraction and a well-characterized chemical leach for labile material. Biogenic PFe was calculated from the measured seasonal mean cellular Fe:C ratios, reported mean C:P at the BATS site and measured labile particulate phosphorus: $\text{PFe}_{\text{bio}} = \text{Fe:C} \times \text{C:P}_{\text{ref}} \times \text{PP}_{\text{labile}}$. The use of a chemical leach for labile material enabled us to define lithogenic PFe operationally as the measured refractory material, $\text{PFe}_{\text{litho}} = \max(0, \text{PFe}_{\text{total}} - \text{Fe}_{\text{labile}})$. We compared this to the more commonly used approach of using aluminium as a proxy for lithogenic material, $\text{PFe}_{\text{litho}} = \text{PAI}_{\text{total}} \times \text{Fe:Al}_{\text{ref}}$, using two reference Fe:Al molar ratios, the mean of all upper continental crust (0.23; ref. 52) and Saharan dust aerosol (0.42; ref. 53). The remaining PFe was defined as authigenic: $\text{PFe}_{\text{auth}} = \max(0, \text{PFe}_{\text{total}} - \text{PFe}_{\text{litho}} - \text{PFe}_{\text{bio}})$.

We also used the GEOTRACES IDP2021 (ref. 54) to explore the potential importance of aFe. We used the IDP2021 observations of labile PFe (assuming that this reflects the actively cycling PFe pool and generally excludes lithogenic PFe) and sought to address whether this pool could be accounted for solely by the commonly considered biogenic PFe pool. To do so, we used IDP2021 labile particulate phosphorus data and a high or low estimate of Fe:P cellular quotas (40 and 10 mmol Fe/mol P). When these different estimates of biogenic PFe were subtracted from the labile PFe, residual or 'missing' PFe was present in half to three-quarters of observations. To avoid biases associated with margin sediments and hydrothermal vents, we conducted this analysis in waters shallower than 2,000 m at stations in which the bottom depths exceeded 3,000 m.

Model equations

Our modelling is based on 'quota' version of the well-established PISCES-v2 model that forms part of the IPSL Earth system model.

PISCES-Quota follows the standard PISCES Quota code⁵⁵, including three phytoplankton groups (picophytoplankton, nanophytoplankton and diatoms), fully decoupled carbon, nitrogen, phosphorus, silica and iron stoichiometry within phytoplankton, dissolved organic and particle pools, with the addition of two aeolian-derived lithogenic particle tracers (fine lithogenic particles and aggregated lithogenic particles) following ref. 56. Fine lithogenic particles sink at 0.5 m day⁻¹ and aggregate to form aggregated lithogenic particles, which sink at 10 m day⁻¹ and disaggregate. The Fe chemistry routines in the PISCES-Quota code assume that all DFe is in equilibrium with ligands (Fig. 2b) and has two minor alterations from the standard PISCES-v2 code⁵⁷: (1) weak total ligands (L_T) are derived from modelled DOC using a default ratio of 0.09 nM L_T (mmol DOC m⁻³)⁻¹ (with extra experiments at 0.08 and 0.07 nM L_T (mmol DOC m⁻³)⁻¹) and (2) a fixed log conditional stability constant of 11 is used to approximate the weaker total ligand pool². PISCES-Quota is also run with prognostic stronger L_1 ligands (see below). In PISCES-Quota, CFe may aggregate (AGG), with a constant stickiness (S) parameter of 0.3, as per the standard PISCES code:

$$\text{AGG} = (A \times \text{DOC} + B \times \text{POC}_S) \times \text{shear} + C \times \text{POC}_S + D \times \text{DOC} + E \times \text{POC}_S + (F \times \text{shear} + G) \times \text{POC}_L \quad (1)$$

in which $A = 12.0 \times S$, $B = 9.05$, $C = 2.49$, $D = 127.8 \times S$, $E = 725.7$, $F = 1.94$ and $G = 1.37$ (all constants are in (mol C l⁻¹)⁻¹ s⁻¹ and from the original PISCES model⁵⁷). POC_S and POC_L refer to small and large particulate organic carbon, respectively. In PISCES-Quota, CFe is assumed to be a fixed 50% component of the FeL pool that dominates DFe (ref. 57). Shear is set to 1 in the mixed layer and 0.01 below.

Aeolian inputs of DFe and fine lithogenic particles are from a 1980–2015 monthly aerosol climatology⁵⁸.

PISCES-Quota-Fe builds on PISCES-Quota, adding two extra particulate authigenic tracers (small and large particulate authigenic Fe). Representing the cycling of colloidal Fe (oxyhydr)oxides out of equilibrium with ligands also required a number of modifications to the Fe chemistry routine.

Empirical calculation of Fe solubility following experimental data⁵⁹ defines sFe. Any DFe in excess of the sFe concentration is assumed to be made up of colloidal Fe (oxyhydr)oxides (CFe or Fe_{ox}). This now means that Fe_{ox} can vary beyond the fixed contribution to DFe assumed previously, consistent with observations. We assume that Fe_{ox} makes a minimum of 10% of DFe. sFe can be complexed by ligands (see below) to produce sFeL, with uncomplexed sFe (sFe') participating in the standard PISCES particle scavenging process (with organic and lithogenic particles; Fig. 2c).

The rate of change in small particulate authigenic Fe (aFe_s):

$$\begin{aligned} d(aFe_s)/dt = & Fe_{ox} \times AGG + Fe_{ox} \times AUTO - aFe_{s_agg} \times aFe_s \\ & - aFe_{s_agg2} \times aFe_L - aFe_{s_diss} \times aFe_s \\ & + aFe_{L_disagg} \times aFe_L \end{aligned} \quad (2)$$

AGG is the specific rate of Fe_{ox} aggregation from the standard PISCES routines⁵⁷. As per equation (1), aggregation of Fe_{ox} is driven by DOC and POC concentrations (aggregation/coagulation with DOC is increased threefold, collf = 3). Interaction of Fe_{ox} with DOC is modulated by an assumed background stickiness of DOC (S, 0.3) and the relative concentration of living biomass (Rbio = Tbio/(Tbio + kbtbio), in which Tbio is the sum of all living phytoplankton and kbtbio = 3 × 10⁻⁸ mol l⁻¹) is a proxy for stickier DOC. Constants modified from equation (1) are: A = 12.0 × S × collf × Rbio and D = 127.8 × S × collf × Rbio (all constants are in (mol C l⁻¹)⁻¹ s⁻¹).

AUTO is a further specific rate that accounts for the autocatalytic aggregation of Fe_{ox} at high concentrations. It is calculated on the basis of a standard Fe_{ox} aggregation rate (0.1 day⁻¹, Fe_{ox_agg}) and a shape function of kcf = 2 nM:

$$AUTO = Fe_{ox_agg} \times Fe_{ox}^4 / (Fe_{ox}^4 + kcf^4) \quad (3)$$

Removal of FeOX through both aggregation with organic carbon and autocatalytic aggregation is a sink for DFe and a source for small authigenic particles (aFe_s).

aFe_s is lost by autocatalytic aggregation (aFe_{s_agg}, accounting for shear) and by interaction with large authigenic Fe (aFe_{s_agg2}, not including shear) to form aFe_L following the assumptions in the standard PISCES particle aggregation code.

aFe_s sinks at 0.5 m day⁻¹ and aFe_s dissolution (aFe_{s_diss}) is set to 1 × 10⁻⁴ day⁻¹.

The rate of change in aFe_L is:

$$\begin{aligned} d(aFe_L)/dt = & aFe_{s_agg} \times aFe_s + aFe_{s_agg2} \times aFe_L - aFe_{L_disagg} \times aFe_L \\ & - aFe_{L_diss} \times aFe_L \end{aligned} \quad (4)$$

and accounts for aggregation of aFe_s (see above) and the disaggregation (aFe_{L_disagg}, 1 × 10⁻³ day⁻¹). aFe_L sinks at 10 m day⁻¹.

For ligands, both PISCES-Quota and PISCES-Quota-Fe can be run with either weaker total ligands (L_T, derived from DOC and a fixed log conditional stability constant of 11) or using the prognostic ligand model for stronger L₁ ligands (with a fixed log conditional stability constant of 12). The prognostic L₁ model is used by PISCES-Quota-Fe as default and is based on the standard PISCES ligand model⁴⁴, with small adjustments to parameter values. Minimum and maximum lifetimes of L₁ ligands are set to 0.2 and 100 years, respectively. The production rates of L₁ ligands from phytoplankton DOC production, zooplankton DOC production and detritus remineralization are set to 1 × 10⁻⁴, 1 × 10⁻⁵ and 5 × 10⁻⁵ mol L₁ mol C⁻¹, respectively. Photochemical loss of L₁ ligands is set to 1 × 10⁻⁴ (W m⁻²)⁻¹ day⁻¹, modulated by a shape function of 1 × 10⁻⁹ mol L₁ l⁻¹. These changes were made to maximize the fit between the modelled and observed L₁ ligands (Extended Data Fig. 1).

Model DFe and PFe distributions were compared with the GEOTRACES IDP2021 dataset³⁴. We binned observations onto the model grid and performed linear regression analysis after log transformation, as in previous model–data assessments¹³. Observations and model solutions for PISCES-Quota and PISCES-Quota-Fe are compared in Extended Data Fig. 4 for ten GEOTRACES ocean transects. We also investigated how the PISCES-Quota model solution compared with the standard version of PISCES in terms of its ability to reproduce the seasonal variations in DFe in Extended Data Fig. 3.

Data availability

Oceanographic data collected and analysed in this study are available at <https://www.bco-dmo.org/project/822807> and <https://www.bco-dmo.org/dataset/888772>.

Code availability

Model code is available at <https://github.com/atagliab/PISCES-BAIT> and output at <https://doi.org/10.5281/zenodo.7378193>.

- Rauschenberg, S. & Twining, B. S. Evaluation of approaches to estimate biogenic particulate trace metals in the ocean. *Mar. Chem.* **171**, 67–77 (2015).
- Twining, B. S. et al. Taxonomic and nutrient controls on phytoplankton iron quotas in the ocean. *Limnol. Oceanogr. Lett.* **6**, 96–106 (2021).
- Rudnick, R. L. & Gao, S. in *Treatise on Geochemistry*, Vol. 3 (eds Holland, H. D. & Turekian, K. K.) 1–64 (Elsevier, 2003).
- Shelley, R. U., Morton, P. L. & Landing, W. M. Elemental ratios and enrichment factors in aerosols from the US-GEOTRACES North Atlantic transects. *Deep Sea Res. II Top. Stud. Oceanogr.* **116**, 262–272 (2015).
- GEOTRACES Intermediate Data Product Group. The GEOTRACES Intermediate Data Product 2021 (IDP2021). <https://doi.org/10.5285/cf2d9ba9-d51d-3b7c-e053-8486abc0f5f6> (NERC EDS British Oceanographic Data Centre NOC, 2021).
- Kwiatkowski, L., Aumont, O., Bopp, L. & Clais, P. The impact of variable phytoplankton stoichiometry on projections of primary production, food quality, and carbon uptake in the global ocean. *Glob. Biogeochem. Cycles* **32**, 516–528 (2018).
- Ye, Y. & Völker, C. On the role of dust-deposited lithogenic particles for iron cycling in the tropical and subtropical Atlantic. *Glob. Biogeochem. Cycles* **31**, 1543–1558 (2017).
- Aumont, O., Ethé, C., Tagliabue, A., Bopp, L. & Gehlen, M. PISCES-v2: an ocean biogeochemical model for carbon and ecosystem studies. *Geosci. Model Dev.* **8**, 2465–2513 (2015).
- Hamilton, D. S. et al. Recent (1980 to 2015) trends and variability in daily-to-interannual soluble iron deposition from dust, fire, and anthropogenic sources. *Geophys. Res. Lett.* **47**, e2020GL089688 (2020).
- Liu, X. & Millero, F. J. The solubility of iron in seawater. *Mar. Chem.* **77**, 43–54 (2002).

Acknowledgements We thank the captains and crews of RV Atlantic Explorer and RV Endeavor and the BATS programme team for their invaluable assistance during the four project cruises. O. Antipova provided assistance in synchrotron data collection and analysis and S. Burns provided assistance with sampling at sea. The model simulations were undertaken on Barkla, part of the High Performance Computing facilities at the University of Liverpool, UK. A.T. and D.K. were supported by NERC award NE/S013547/1; P.S. and B.S. were supported by NSF award OCE-1829833; B.S.T., D.C.O. and L.E.S. were supported by NSF award OCE-1829819; K.N.B. and S.C. were supported by NSF award OCE-1829777; R.J. was supported by NSF award OCE-1829844. This research used resources of the Advanced Photon Source, a U.S. Department of Energy (DOE) Office of Science user facility operated for the DOE Office of Science by Argonne National Laboratory under contract no. DE-AC02-06CH11357.

Author contributions The overarching BAIT programme was conceptualized by P.S., K.N.B., R.J., A.T., D.C.O. and B.S.T. Field and laboratory work was conducted by K.N.B., S.C., R.J., D.C.O., L.E.S., B.S., P.S., A.T. and B.S.T. This study was designed and led by A.T., alongside K.N.B., L.E.S. and B.S.T., with further contributions from O.A., P.W.B., W.B.H. and P.S. Analysis of dissolved iron, ligands and particles was performed by P.S. and B.S., K.N.B. and S.C., and L.E.S. and B.S.T., respectively. Modelling work was undertaken by A.T. Data synthesis and model-data comparisons were conducted by A.T., D.K. and L.E.S. A.T. led the drafting of the manuscript, with input from all co-authors.

Competing interests The authors declare no competing interests.

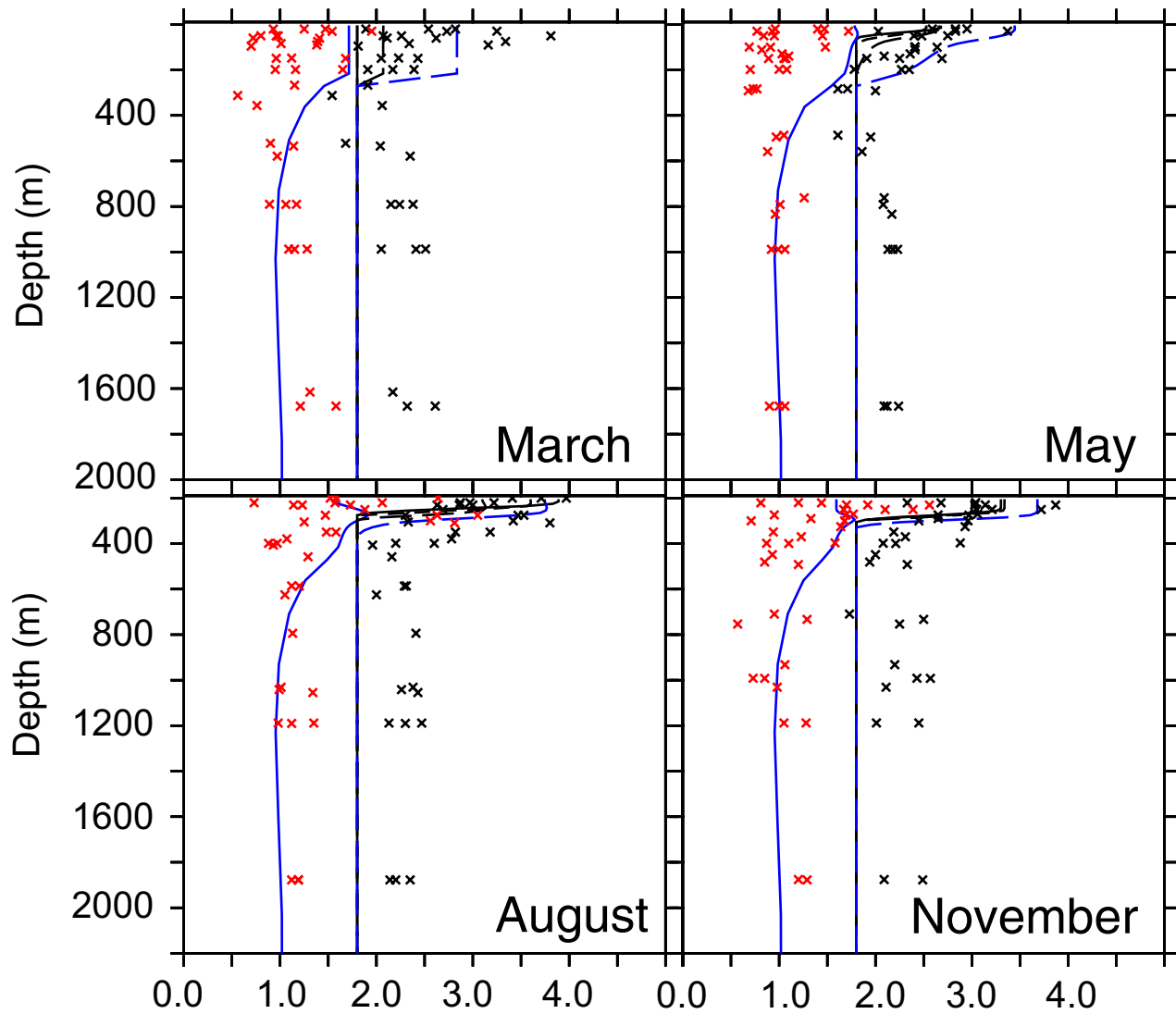
Additional information

Supplementary information The online version contains supplementary material available at <https://doi.org/10.1038/s41586-023-06210-5>.

Correspondence and requests for materials should be addressed to Alessandro Tagliabue.

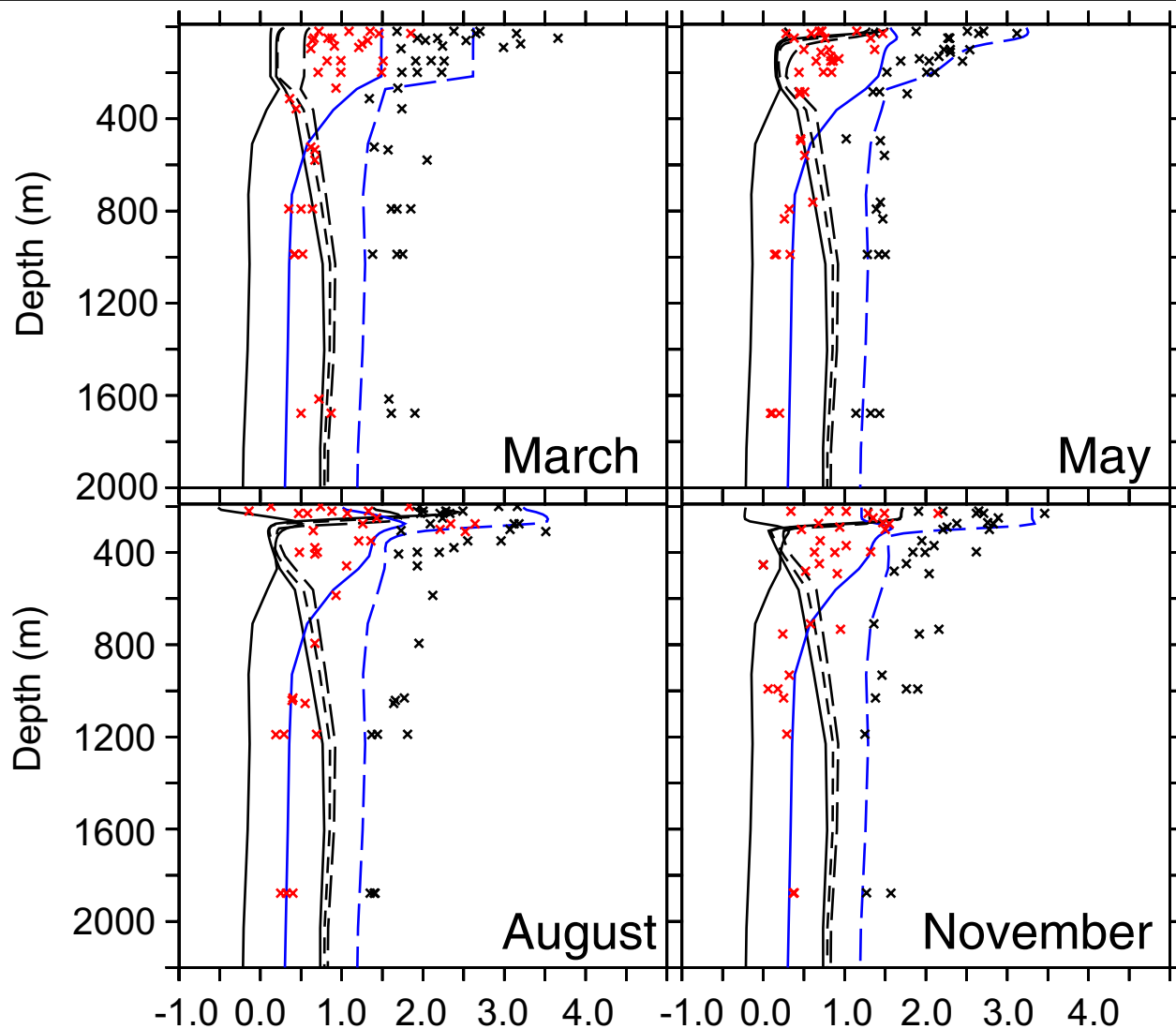
Peer review information *Nature* thanks Kazuhiro Misumi, Brandy Toner and the other, anonymous, reviewer(s) for their contribution to the peer review of this work.

Reprints and permissions information is available at <http://www.nature.com/reprints>.



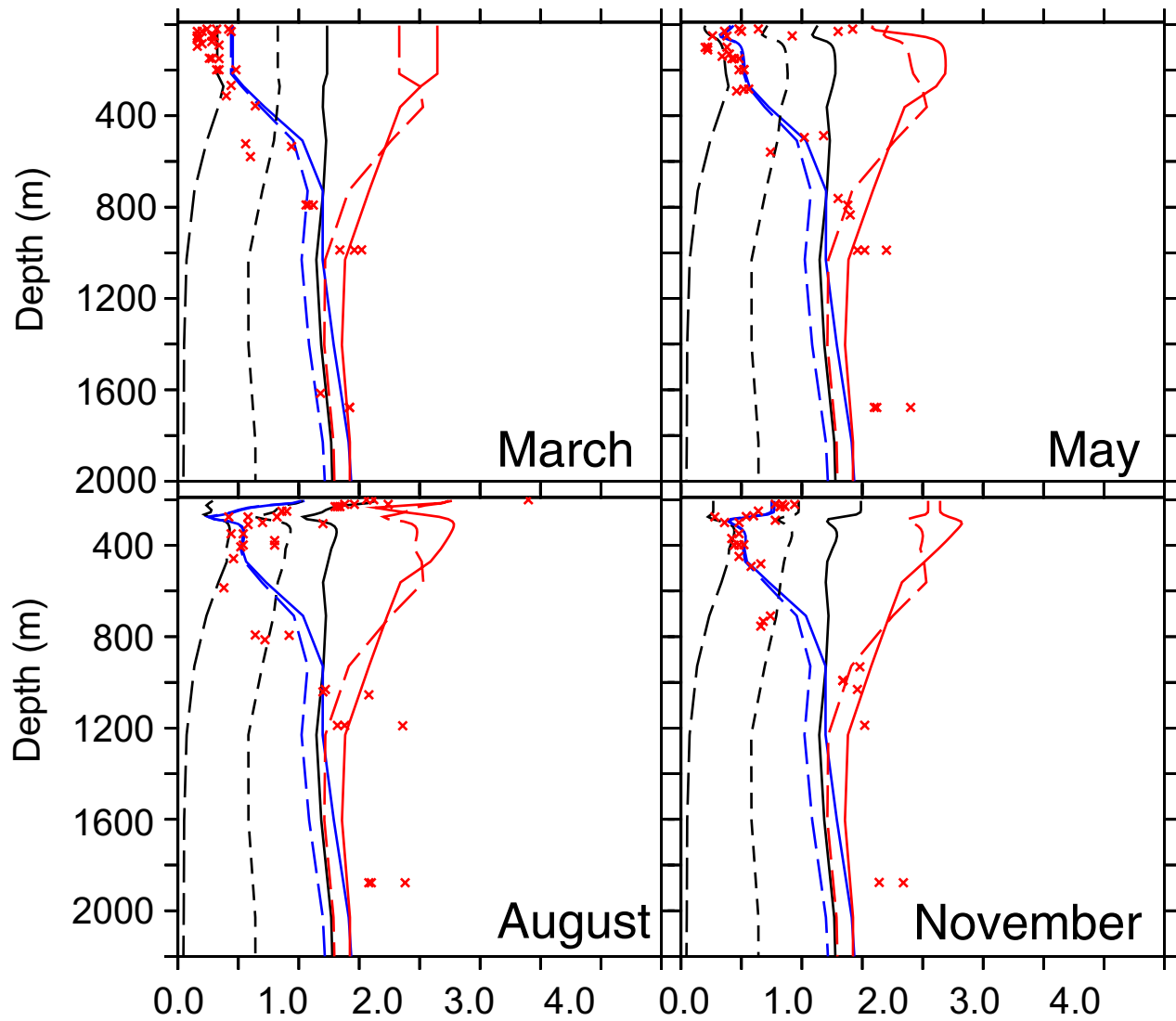
Extended Data Fig. 1 | Seasonal evolution of total and stronger ligands. Observed and modelled total (black symbols) and stronger (red symbols) ligand concentrations (nM). Black lines are model solutions at the BATS site from the PISCES-Quota model, with varying total ligands derived from DOC

(using 0.09, 0.08 and 0.07 nM $L_T \mu\text{M DOC}^{-1}$). Blue lines represent model solutions from PISCES-Quota-Fe, with either prognostic stronger ligands (solid line) or DOC-derived total weaker ligands (dashed line, using 0.09 nM $L_T \mu\text{M DOC}^{-1}$).



Extended Data Fig. 2 | Seasonal evolution of excess ligands. Observed and modelled excess total (black symbols) and strong (red symbols) ligands (both in nM). Solid and dashed black lines are model solutions at the BATS site from the PISCES-Quota model, with varying total ligands derived from DOC (using 0.09, 0.08 and 0.07 nM L_T ($\mu\text{M DOC}^{-1}$) or prognostic stronger ligands (thin

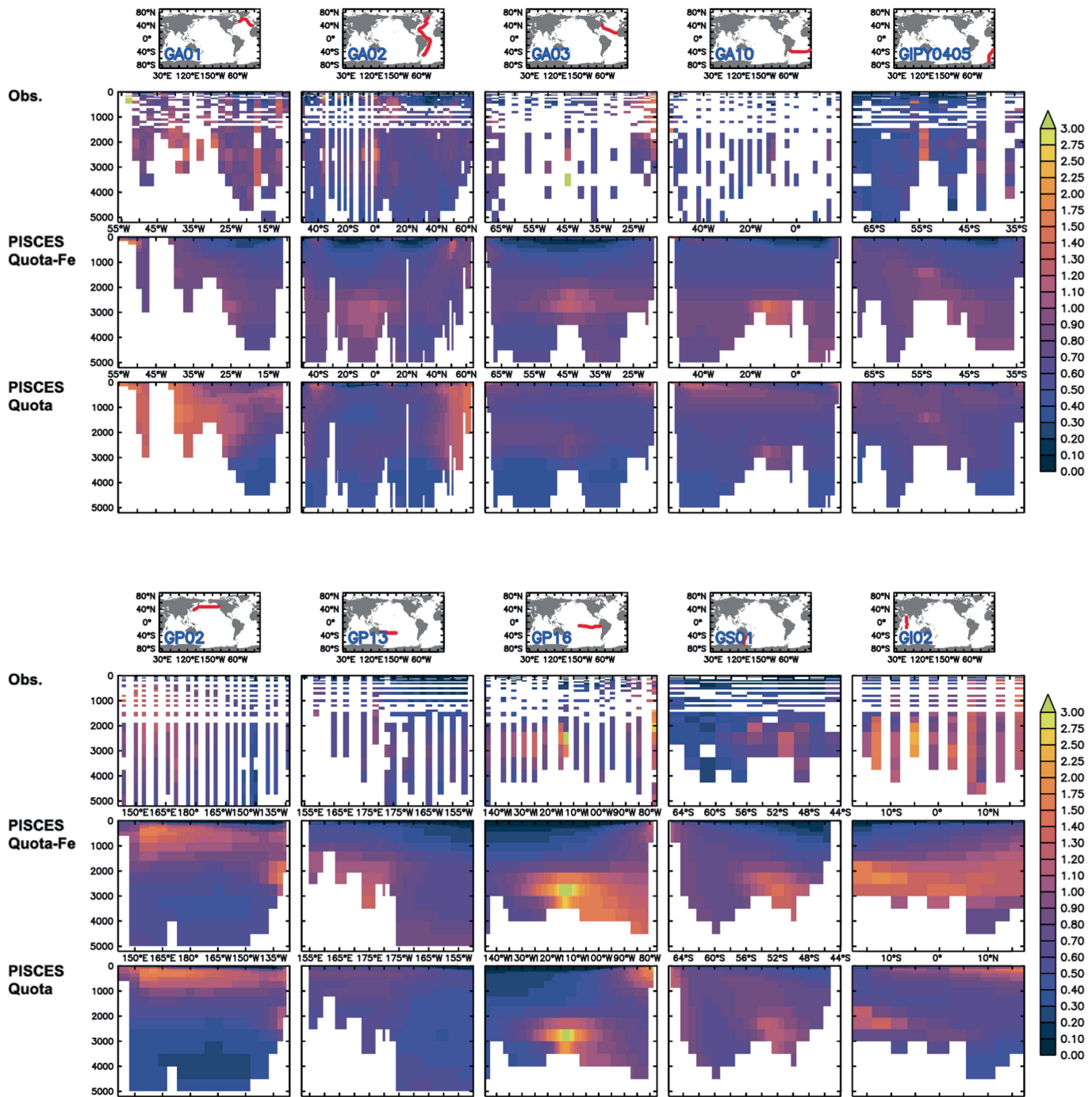
black lines). Blue lines represent model solutions from PISCES-Quota-Fe, with either prognostic stronger ligands (solid line) or DOC-derived total ligands (dashed line, using 0.09 nM L_T ($\mu\text{M DOC}^{-1}$)). Values less than zero are when DFe concentrations exceed the concentrations of either L_1 or L_T . Only the PISCES-Quota-Fe model is able to generate the observed large excess ligand pools.



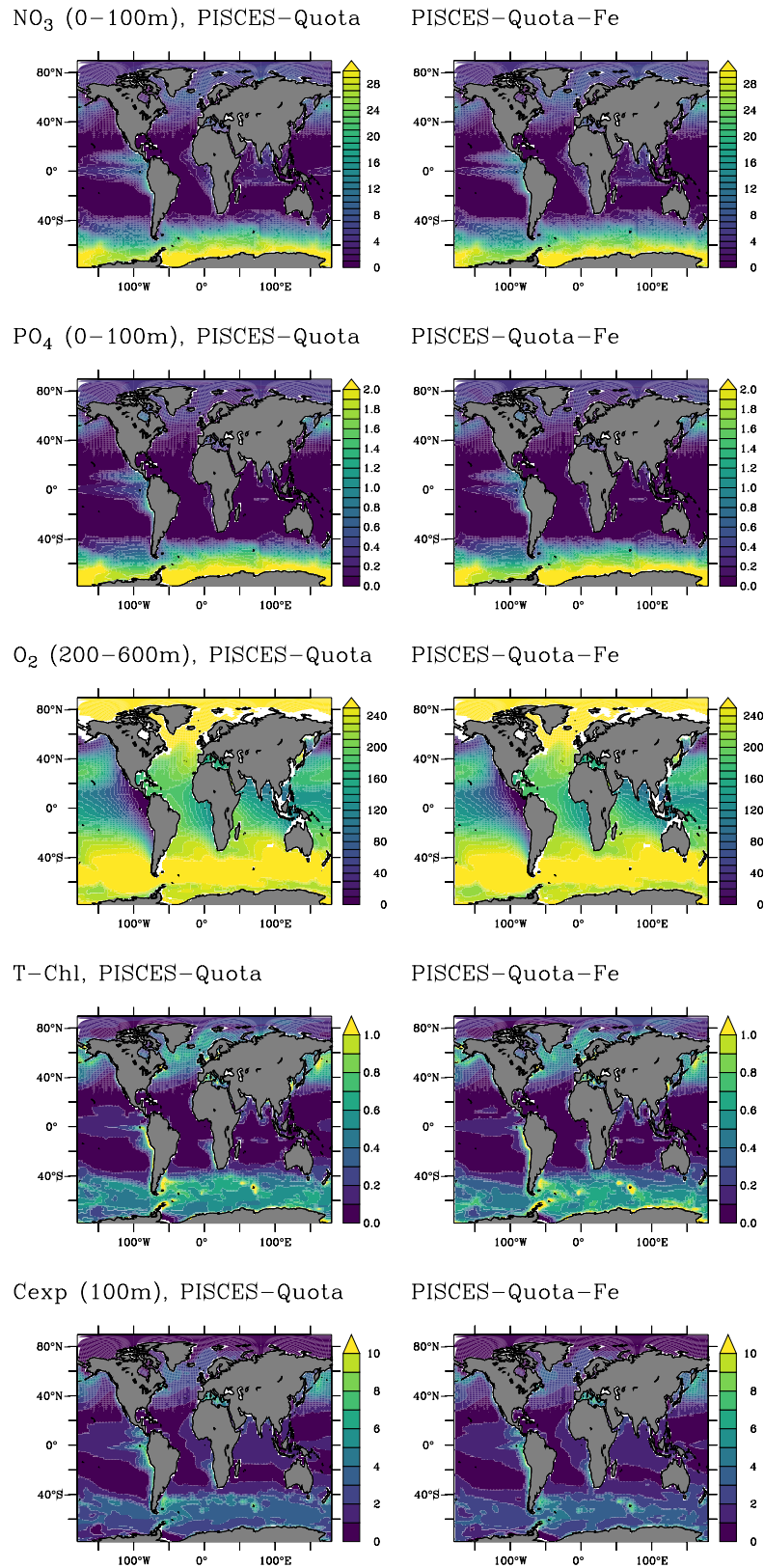
Extended Data Fig. 3 | Variations in the seasonal evolution of dissolved iron.

DFe data and model solutions at the BATS site. Red crosses are DFe data for each voyage for three stations in the BATS region. All black lines are model solutions at the BATS site from the PISCES-Quota model, with total ligands derived from DOC (using $0.09 \text{ nM L}_T \mu\text{M DOC}^{-1}$) but with varying strengths of scavenging of free Fe by lithogenic particles. Blue lines represent model solutions from the new PISCES-Quota-Fe model, with either prognostic

stronger ligands (solid line) or DOC-derived total ligands (dashed line, using $0.09 \text{ nM L}_T (\mu\text{M DOC})^{-1}$). In red, we also compare the default PISCES-Quota (solid line, with total ligands derived from DOC using $0.09 \text{ nM L}_T \mu\text{M DOC}^{-1}$) and PISCES standard (dashed line) models. This demonstrates that there is little difference in the model–data mismatch in the seasonal evolution of DFe between PISCES-Quota and the standard PISCES model.



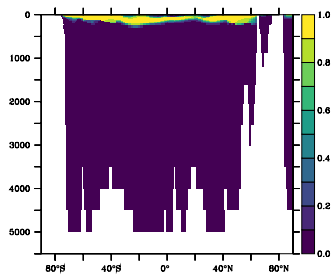
Extended Data Fig. 4 | Global model-data comparison of dissolved iron. Observed and modelled dissolved iron (nM) for ten GEOTRACES sections for PISCES-Quota-Fe and PISCES-Quota. Observations and models are binned onto the same vertical grid.



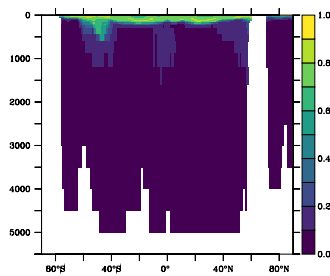
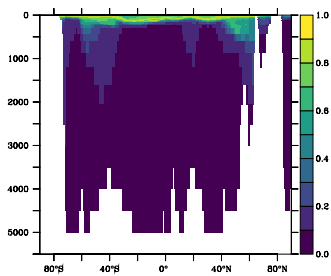
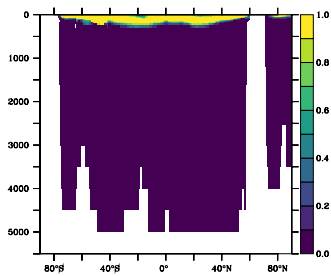
Extended Data Fig. 5 | Model performance for biogeochemical metrics. Plots showing the difference in performance between PISCES-Quota and PISCES-Quota-Fe for a suite of biogeochemical diagnostics. Average upper 100 m NO₃ and PO₄ are in mmol m⁻³, average 200–600 m O₂ is in mmol m⁻³, total

chlorophyll (T-Chl) at the surface (summed across the picophytoplankton, nanophytoplankton and diatoms) is in mg m⁻³ and carbon export at 100 m is in mol m⁻² year⁻¹. It can be seen that the new PISCES-Quota-Fe model does not substantially alter the biogeochemical mean state of the model.

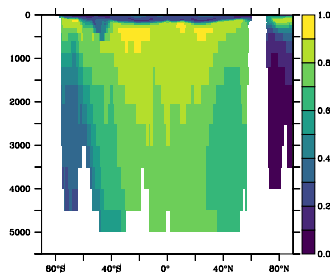
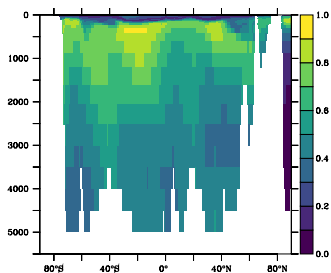
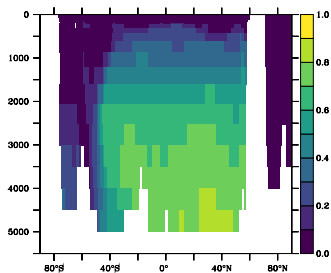
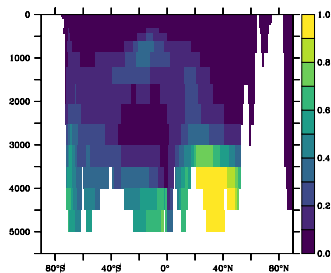
Phytoplankton Fe Uptake



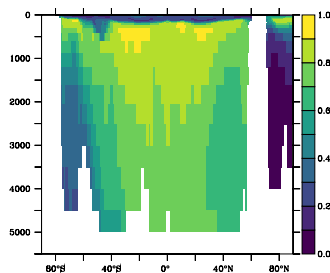
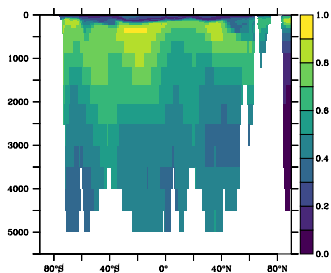
Zooplankton Fe Recycling



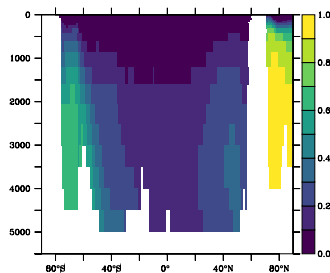
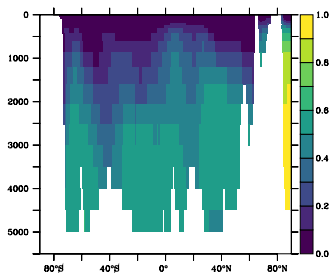
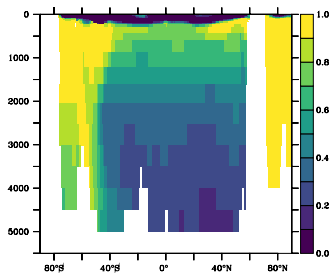
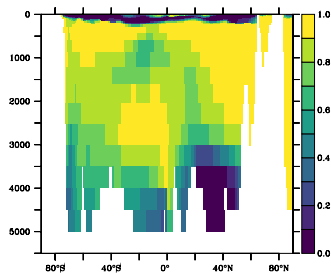
Fe Scavenging



Fe Regeneration



Iron Oxide Aggregation to > 0.2um



Atlantic (20W)

Pacific (150W)

Atlantic (20W)

Pacific (150W)

Extended Data Fig. 6 | Iron cycle fluxes in the Atlantic and Pacific oceans. Proportional contributions of different processes to total DFe supply and removal fluxes along two example sections in the Atlantic (20° W) and Pacific (150° W) oceans from the PISCES-Quota-Fe model with prognostic strong ligands.

Article

Extended Data Table 1 | Model–observations statistical assessment

	Depths	Exp.	Nr. of obs.	Obs mean	Model mean	Bias	Slope	R
DFe	Full Depth	PISCES-Quota-Fe	10743	0.37	0.43	0.06	0.8	0.59
		PISCES-Quota			0.63	0.26	0.32	0.41
	Upper 200m	PISCES-Quota-Fe	4545	0.22	0.21	-0.01	0.78	0.51
		PISCES-Quota			0.56	0.34	0.45	0.49
PFe	Full Depth	PISCES-Quota-Fe	1664	0.85	0.48	-0.37	0.7	0.59
		PISCES-Quota			0.28	-0.58	0.39	0.3
	Upper 200m	PISCES-Quota-Fe	687	0.66	0.38	-0.28	0.48	0.47
		PISCES-Quota			0.28	-0.39	0.25	0.24

Summary statistics for dissolved and particulate Fe across the PISCES-Quota-Fe and PISCES-Quota models for full depth and the upper 200 m using data compiled from the GEOTRACES IDP2021. We report the number of observations, model and observation mean (all in nM), bias and the slope and correlation coefficient (*R*) for log-transformed analysis. In all cases, PISCES-Quota-Fe has a lower bias, better correlation and shows a slope closer to 1.0, indicating improved performance. Persistent biases in PFe reflect missing extra lithogenic PFe sources.